MATERIALS SCIENCE

High-strength and fracture-resistant ionogels via solvent-tailored interphase cohesion in nanofibrous composite networks

He Zhang[1,2]†, Weibin Jia[3,4]†, Mingze Sun[1], Yuxiang Chen[1], Xiaoyi Zhang[1,2], Hao Li[1], Xingdao He[3,4], Peng Shi[3,5,4]*, Lizhi Xu[1,2,6]*

Ionogels are promising for soft robotics, energy systems, and bioelectronic interfaces due to their high ionic conductivity and environmental stability. However, combining high strength and fracture resistance remains challenging. Here, we report composite ionogels with outstanding mechanical strength (~65.4 megapascal) and fracture energy (~607 kilojoules per square meter), capable of bearing more than 5000 times their own weight. These ionogels are developed by tailoring solvent-solute interactions to create a dense, hyperconnected nanofibrous polymer network. Solvent engineering regulates hydrogen bonding competition, facilitating the formation of robust interphase hydrogen bonds and a soft-hard biomimetic interface. Moreover, their antidrying, breathable nature enables multifunctional electrophysiological monitoring, making them ideal for wearable bioelectronics. Their ionic conductivity, drug-loading capacity, and antibacterial properties allow their use in advanced e-bandages for chronic wound healing. This generalizable strategy for ionogel design opens pathways toward strong, versatile, and biocompatible materials, particularly valuable for next-generation soft materials, wearable electronics, and tissue engineering.

INTRODUCTION

Ionogels typically feature three-dimensional (3D) polymeric networks packaged by ionic liquids that maintain their shape and structural integrity. Because of the excellent flexibility, intrinsic ionic conductivity, and environmental stability (e.g., nonvolatility and antifreezing behavior), ionogels have found broad applications in soft robotics (*1*–*3*), energy storage and conversion devices (*4*–*7*), bioprostheses (*8*), tissue engineering (*9*–*11*), bioelectronic interfaces (*12*–*15*), and other advanced technologies. Beyond these wide functional explorations, there are also continuous efforts in seeking ionogels of improved mechanical robustness, particularly high strength and fracture energy. Most existing systems fall short in either of these regards, with typical fracture strength below 1 MPa and fracture energy under 1 kJ/m^2, which limits the reliability and broader applicability of ionogel materials.

Composite designs represent an efficient strategy for enhancing the mechanical performance (*16*–*18*). Nature has combined disparate components to form architectures featuring exceptional fracture resistance and tensile strength, as nicely exemplified by the flexible wing membranes of insects and nacre (*19*, *20*). Despite extensive research on multiphasic ionogel design, simultaneously enhancing the strength and fracture energy to match those of natural materials remains challenging, typically requiring a classical trade-off between the two (*21*, *22*). For example, representative double-network (DN) ionogels improve fracture energy by introducing sacrificial bonds that effectively dissipate mechanical energy (*23*); however, their fracture strength remains limited to only a few hundred kilopascals. Ionogels comprising two distinct phases with contrasted modulus have attracted growing attention because of their ability to mimic the hierarchical organization of natural composites (*24*, *25*). Nonetheless, realizing high fracture energy in these systems is still difficult, largely because of the weak interfacial interactions between the disparate phases—interactions that are crucial for efficient load transfer (*26*).

Here, we develop high-strength and fracture-resistant ionogels (HSFRIs) through solvent-engineered interfacial cohesion in a biphasic soft-hard structure. Solvents, such as water, that form strong hydrogen bonds with solid components can disrupt polymer chains and weaken soft-hard phase interactions, ultimately resulting in soft and fragile gels (*27*). To address this, we tailor the solute-solvent interactions to reduce the solvent's competition for hydrogen bonding sites, thereby preserving internal hydrogen bonds within the two phases in the solute. This approach can be used to achieve robust interfacial cohesion, producing ionogels with both high strength and fracture energy. As a demonstration, we fabricated HSFRIs by combining aramid nanofibers (ANFs) as the hard phase and polyvinyl alcohol (PVA) as the soft phase in 1-ethyl-3-methylimidazolium trifluoromethanesulfonimide (EMIMTFSI). This design mimics natural composite materials like insect wing membranes and nacre, featuring an exceptionally strong interface between two phases with a large modulus contrast. Suppression of solvent-solute hydrogen bonds promotes interfacial hydrogen bond formation within the solute, thereby enhancing physical interactions between ANFs and PVA (Fig. 1A). This leads to the formation of a dense, hyperconnective nanofibrous 3D network (Fig. 1B), rendering mechanical performance improvements several orders of magnitude greater than those of conventional hydrogels (Fig. 1C). The resulting ionogels exhibit exceptional fracture strength (64.5 MPa) and fracture energy (~607 kJ/m^2), capable of

[1]Department of Mechanical Engineering, The University of Hong Kong, Hong Kong, SAR, China. [2]Advanced Biomedical Instrumentation Centre Limited, Hong Kong, SAR, China. [3]Department of Biomedical Engineering, College of Biomedicine, City University of Hong Kong, Hong Kong, SAR, China. [4]Hong Kong Centre for Cerebro-Cardiovascular Health Engineering, Hong Kong Science Park, Hong Kong, SAR, China. [5]Center of Super-Diamond and Advanced Films (COSDAF), City University of Hong Kong, Hong Kong, SAR, China. [6]Materials Innovation Institute for Life Sciences and Energy (MILES), The University of Hong Kong Shenzhen Institute of Research and Innovation (HKU-SIRI), Shenzhen, China.
*Corresponding author. Email: xulizhi@hku.hk (L.X.); pengshi@cityu.edu.hk (P.S.)
†These authors contribute equally to this work.

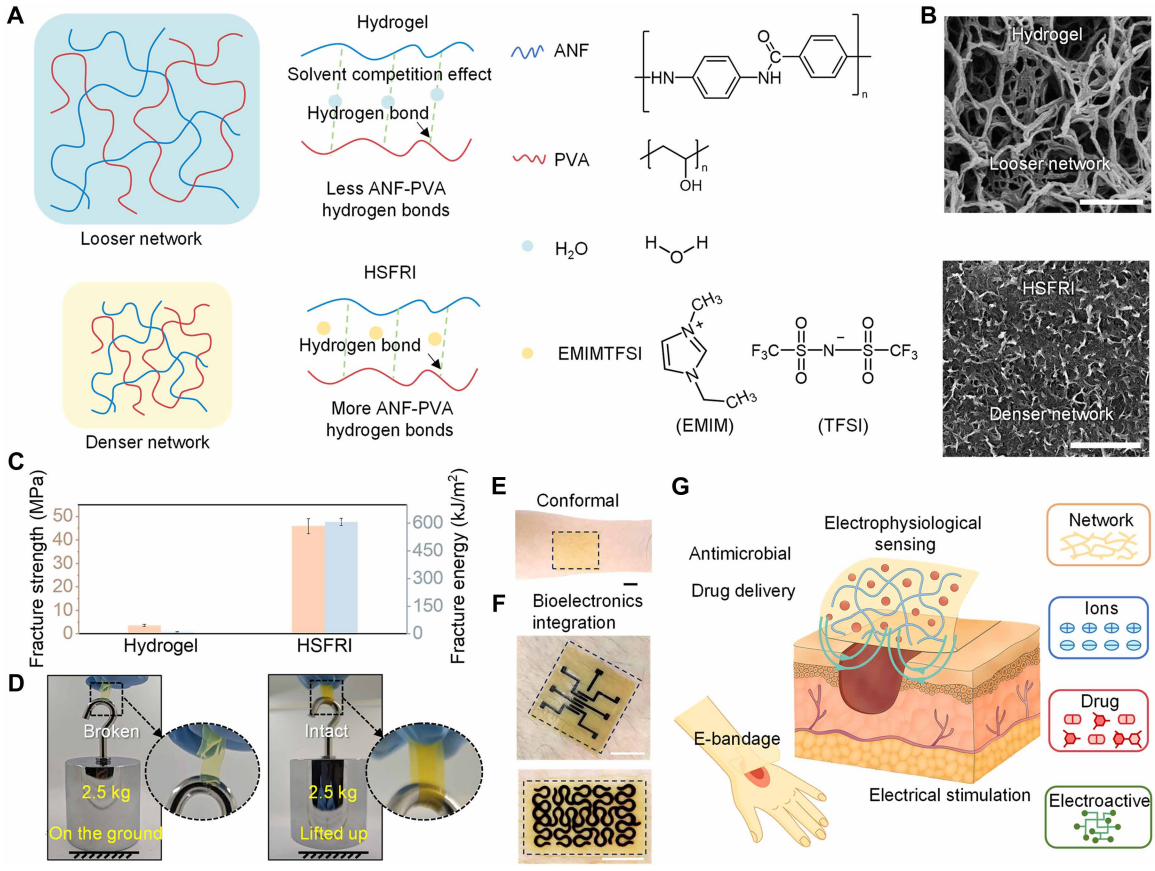

Fig. 1. Design and implementation of the HSFRIs. (**A**) Schematic illustration of the polymeric network swollen in water (top) and EMIMTFSI (bottom). The weaker hydrogen bonding ability of the EMIMTFSI favors the formation of more hydrogen bonds between ANFs and PVA, leading to a robust interphase cohesion and yielding HSFRIs. (**B**) SEM characterization of the microstructures of the hydrogel (top) and HSFRIs (bottom) reveals a denser and more interconnected network in HSFRIs. (**C**) Comparison of tensile strength and fracture energy between the hydrogel and HSFRIs, both derived from the same ANF-PVA precursor. (**D**) Photographs showing a hydrogel (left) and HSFRIs (right) lifting a 2.5-kg weight. The hydrogel fractures, whereas the HSFRIs successfully bear the load. (**E**) Photograph showing the conformal integration of HSFRIs with skin. (**F**) Patterned PPy electrodes integrated into HSFRIs serve as monolithic, skin-interfaced bioelectronic platforms. Scale bars, 1 cm. (**G**) Schematic illustration of an HSFRIs-based e-bandage. The antibacterial properties, hydrophobic drug–loading capacity, and ionic conductivity of HSFRIs underscore their potential as dressing bandages for next-generation wound care.

supporting at least 5000 times their own weight (Fig. 1D). The structural stretchability and deformability of the ionogels allow conformal integration with 3D biological surfaces (Fig. 1E). Moreover, the excellent processability of HSFRIs enables in situ incorporation of conducting polymer patterns into multifunctional bioelectronic interfaces (Fig. 1F). Notably, the unique solvent system permits the delivery of water-insoluble drugs and, in combination with its intrinsic ionic conductivity (6.5 mS/m) and antibacterial properties, providing the ionogel with considerable versatility as a biomedical platform—for instance, as an e-bandage for wound healing (Fig. 1G).

RESULTS

Synthesis and mechanical properties of HSFRIs

Our design for HSFRIs involves dispersing stiff ANFs within a soft PVA matrix, which is formed through a one-step solvent-exchange process from dimethyl sulfoxide (DMSO) to the target liquids (fig. S1). The transition from a liquid precursor to a solid iongel is driven by hydrogen bond formation between the hydroxyl groups of PVA and the carbonyl groups of ANFs (fig. S2). The film morphology with thin thickness created by the blade-coating process ensures a homogeneous gelation process and a uniform internal microstructure. It is conceivable that the target solvent can significantly influence the gelation behavior during the solvent exchange process. First, miscibility between the target and original solvents is essential for smooth exchange and uniform polymeric network formation. Second, the target solvent is expected to enhance intermolecular interactions between polymer chains to facilitate the formation of an interconnected network and induce gelation. Third, there needs to be sufficient affinity between the solvent and polymer to retain an adequate liquid fraction, allowing the material to remain in a stretchable gel state. Notably, however, the excessive hydrogen-bonding affinity of the solvent may lead to competition with both phases, thereby diminishing their interfacial cohesion.

To examine the influence of solvents on the mechanical properties of the resulting gels, we selected three representative solvents—water, 1-ethyl-3-methylimidazolium tetrafluoroborate ($EMIMBF_4$), and EMIMTFSI—corresponding to strong, moderate, and weak hydrogen bond formation capabilities, respectively (*28*). The mechanical response of the gels swollen in the three solvents was evaluated, with

the initial mass ratio of ANFs to PVA maintained at 2:15 (Fig. 2A). It was found that the mechanical properties improved significantly as the solvent's hydrogen bond formation capability decreased. The HSFRIs exhibited an impressive ultimate tensile strength of approximately 46 MPa and fracture energy of around 607 kJ/m^2, which are 12.6 times and 54.4 times higher, respectively, than those of the hydrogel with water as the solvent (Fig. 2B and fig. S3). The increased strain further highlights the high liquid content (~63%) in HSFRIs, indicating a strong affinity between EMIMTFSI and the solid phase. Notably, even with the same solid fraction, HSFRIs show a 6.4-fold improvement in mechanical strength compared to hydrogels (fig. S4).

The mechanical properties of the HSFRIs are strongly influenced by the proportion of the hard phase. We prepared HSFRIs derived from liquid precursor with mass ratios of ANF to PVA ranging from 0:15 to 3:15. As the ANF content slightly increased, the fracture strength of the HSFRIs significantly improved, while the strain and fracture energy decreased (Fig. 2C and fig. S5). For example, when the mass ratio increased to 3:15, the HSFRIs achieved their highest fracture strength (~64.5 MPa), with a slight decrease in both fracture energy and strain (Fig. 2D). Moreover, our approach of integrating separated phases through solvent interaction regulation provides a universal strategy for the straightforward fabrication of physically robust ionogels. For instance, in addition to ANFs, the hard phase can be replaced with other polymer fibers such as cellulose or silk fibroin. Similarly, commonly used polysaccharides like chitosan serve as excellent alternatives to PVA for the soft phase (Fig. 2E and fig. S7). This method thus allows for the efficient fabrication of a wide range of ionogels with mechanical properties that exceed those of hydrogels with the same solute composition by one to two orders of magnitude. The HSFRIs exhibit exceptional fracture energy and strength, outperforming other high-performance gels, including those reinforced by DN, phase separation, and various other strengthening mechanisms (Fig. 2F and table S1) (*23*–*25*, *29*–*45*). Notably, HSFRIs have strength and toughness comparable, or

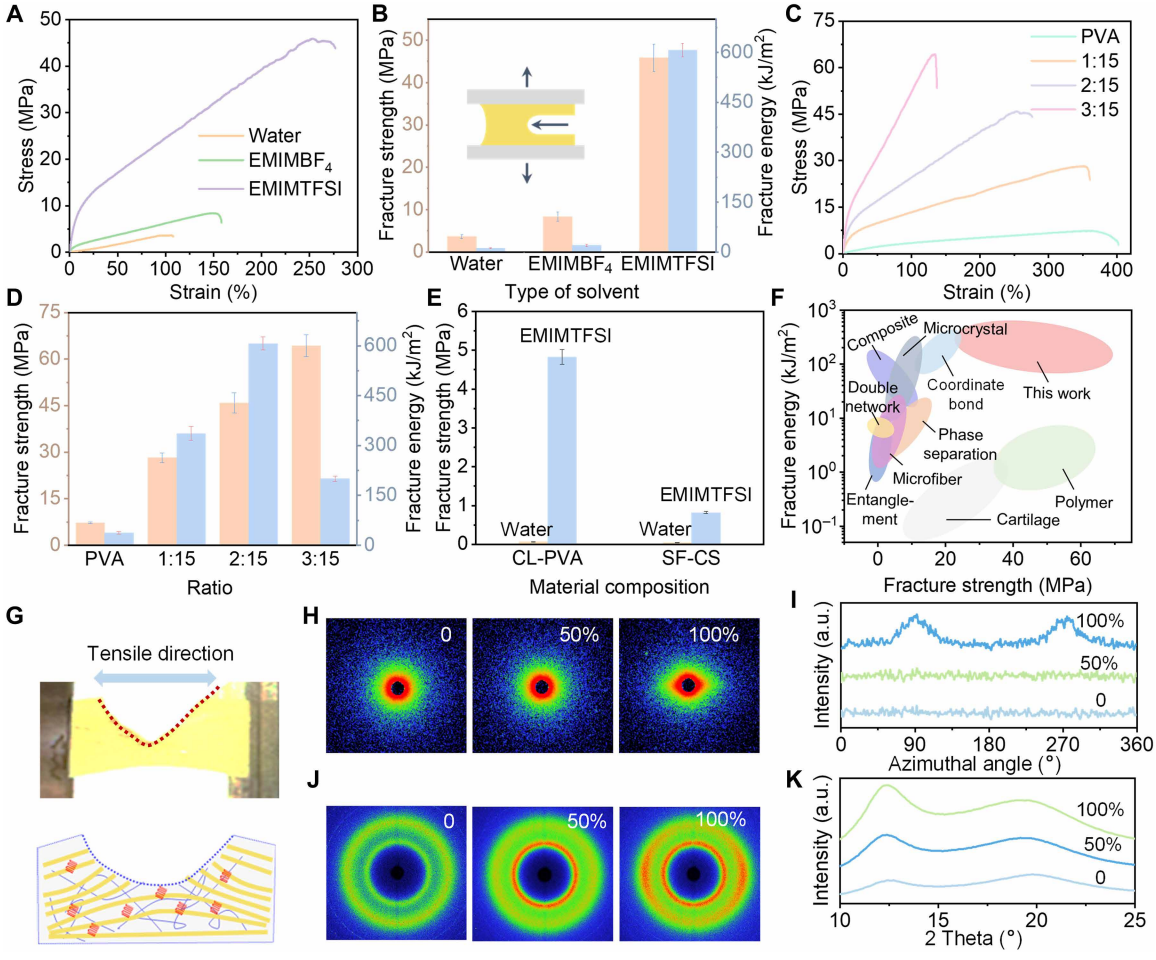

Fig. 2. Mechanical properties of HSFRIs. (**A**) Tensile responses of gels swollen in different solvents with varying hydrogen bonding abilities: water > $EMIMBF_4$ > EMIMTFSI. (**B**) Comparison of fracture strength and energy of gels swollen in different solvents. (**C**) Tensile response of HSFRIs with varying initial ANF-to-PVA ratios. (**D**) Comparison of fracture strength and energy of HSFRIs with different initial ANF-to-PVA ratios. (**E**) Comparison of fracture strength of gels with different solvents (water and EMIMTFSI) in cellulose (CL)–PVA and silk fibroin (SF)–chitosan (CS) composites. Ionogels show markedly higher fracture strength and energy than hydrogels, demonstrating solvent engineering as a generalizable strategy. (**F**) Fracture energy and strength of this work in comparison with cartilage, gels, and polymers (see details in table S1). (**G**) Schematic illustration of the alignment and crystallization behaviors of HSFRIs under stretching. (**H**) Small-angle x-ray scattering profiles of HSFRIs under different strains (0, 50, and 100%). (**I**) Azimuthal intensity analysis of HSFRIs at various strain levels (0, 50, and 100%), indicating increasing orientation of the nanofibers during stretching. [(I) to (K)] 1D curves (**J**) and 2D patterns (**K**) of wide-angle x-ray scattering (WAXS) of HSFRIs under different strains (0, 50, and 100%). a.u., arbitrary units.

even exceeding, those of engineering plastics such as polycarbonate, while offering an order of magnitude higher elongation and a modulus that is two orders of magnitude lower. These characteristics allow HSFRIs to be easily folded and twisted, which is crucial for developing biodevices with high mechanical durability and adaptability to deformation (fig. S8).

Another key feature of HSFRIs is their resistance to crack propagation, as evidenced by the blunting of the crack tip (Fig. 2G). This property is closely linked to the evolution of the microstructure, as characterized by in situ small-angle x-ray scattering and wide-angle x-ray scattering. During the step-by-step tensile loading ($\varepsilon = 50\%$), the orientation of ANFs along the stretching direction becomes more pronounced (Fig. 2, H and I, and fig. S9), which is essential for dissipating strain energy and enhancing fracture energy. The increased peak intensity and decreased full width at half maximum of the (101) plane of PVA with increasing strain indicate progressive crystallization (Fig. 2, J and K, and fig. S10) and reduced grain size, illustrating the transformation of amorphous chain segments into nanocrystalline microregions. The synergistic effect of stretching-induced alignment of the hard phase and the crystallization of the soft phase plays a crucial role in preventing crack propagation (fig. S11) (*46*, *47*).

Toughen mechanism by tailoring solvent-solute interactions

The stark contrast in the mechanical response between hydrogels and HSFRIs highlights the crucial role of solvent effects. It is proposed that tuning the solvent interaction energy enhances the physical binding energy between ANFs and PVA. Strong hydrogen bonding between ANFs and PVA is evidenced by Fourier transform infrared (FTIR) spectroscopy (Fig. 3A), where the stretching vibration of ANFs' carbonyl group (C═O) in the hydrogel at 1642 cm^{-1} shifts to 1650 cm^{-1} in HSFRIs (*48*). To further explore hydrogen bond formation between ANFs and PVA in different solvent environments, molecular dynamics simulations were conducted. A computational model was constructed using the same solute composition, maintaining an ANFs-to-PVA mass ratio of 2:15 (fig. S12). To closely replicate the experimental conditions of both hydrogels and HSFRIs, the solute molecules were randomly inserted into two different solvents: water and EMIMTFSI. The hydrogen bonds between ANFs and PVA formed rapidly and stabilized within 100 ns in both systems (Fig. 3E and fig. S13). Compared to hydrogels, HSFRIs exhibited three times as many hydrogen bonds between ANF and PVA (Fig. 3B), which is critical for establishing a physically robust, separated-phase interface. In contrast, solvent-solute (sum of solvent-ANFs and solvent-PVA) hydrogen bonding was over ~170% higher (fig. S14). These results highlight the competitive effect of the solvent on hydrogen bond formation. In addition, calculations of solute-solvent interaction energy revealed a significantly higher interaction energy in EMIMTFSI-solute systems compared to water-solute systems. This can be attributed to the stronger electrostatic interactions in the ionic liquid, owing to its higher ionized concentration (Fig. 3C). Furthermore, π-π interactions between the aromatic rings in EMIMTFSI and ANF further enhance their mutual affinity (Fig. 3D). Notably, these physical interactions do not interfere with hydrogen bond formation between ANF and PVA; instead, they contribute to maintaining a high liquid content in the gel material. Meanwhile, the substantial shrinkage of the HSFRI network, as observed through scanning electron microscopy (SEM), further confirms that the strong physical interaction between ANF and PVA leads to a denser microstructure (Fig. 1, A and B).

In sum, these findings demonstrate that HSFRIs exhibit a reinforcement mechanism driven by solvent-solute interactions (Fig. 3F). Hydrogen bonds act as cross-linkers, bridging the rigid ANF phase and the flexible PVA phase, with their quantity dictating the transition of the gel from weak to strong. In hydrogels, the competitive effect of the solvent reduces the number of hydrogen bonds between ANF and PVA, resulting in lower strength and fracture energy. In contrast, HSFRIs form an engineering polymer-like strong and tough gel due to an increased number of hydrogen bonds that physically cross-link the separated phases. Furthermore, the presence of intermolecular interactions, such as electrostatic forces and π-π interactions, helps retain sufficient solvent within the polymer network, ensuring exceptional gel-like stretchability. The enhanced interaction between ANF and PVA promotes polymer conformation rearrangement and induces PVA crystallization (Fig. 3, G and H, and fig. S15). These resulting crystalline domains act as stiff cross-linking points, increasing the rigidity of the molecular chains and effectively pinning cracks, thereby further strengthening and toughening HSFRIs.

Applications in bioelectronic interfaces

The outstanding mechanical performance of HSFRIs provides favorable processability for integrating multifunctional electronics and facilitates the establishment of bioelectronic interfaces (Fig. 4A). For example, conducting polymers, such as polypyrrole (PPy), can be in situ polymerized into HSFRIs as a wearable bioelectrode. In combination with a mask, polymerization can be restricted to specific areas, thereby defining the precise patterns of electrodes and interconnects (fig. S16). Furthermore, the ultrathin film structure (~20 μm) enables the conformal integration with skin (Fig. 4B).

Compared to devices based on other substrates, bioelectronics made from HSFRIs show distinct advantages. Antidrying capacity is an important index for long-term epidermal electronics. Because of the antievaporation property of ionic liquids in HSFRIs, their mass remains virtually unchanged even after a week of exposure to the atmosphere (Fig. 4C). In contrast, the hydrogel dried out rapidly within 12 hours, with its water content significantly decreasing by as much as 82.1% after just 24 hours of storage (fig. S17). The fibrous network and ultrathin film structure provide HSFRIs with exceptional gas permeability, an essential attribute for the breathability of epidermal electronics. As a result, they achieve a high water vapor transmission rate (WVTR) of 472 g m^{-2} day^{-1}, 15 times that of commercial polydimethylsiloxane (PDMS) films (Fig. 4D). Although HSFRIs have a denser polymer nanofiber network than hydrogels, they still have intrinsic pores that enable gas transport. Their breathability surpasses that of conventional polymer substrates such as PDMS, supporting their application in epidermal electronics. High charge storage capacity (CSC) is essential for effective signal transmission between electronic devices and biological systems. The PPy-HSFRI electrode achieved a remarkably high CSC of 69.4 mC/cm^2, which is 125 times higher than that of the Au-PDMS electrode (0.56 mC/cm^2) (fig. S18). The antifreezing properties of EMIMTFSI contribute to the stable operation of HSFRI-based epidermal electronics in low-temperature environments, whereas the hydrogel becomes frozen, turning into a hard and brittle state (fig. S19).

We used the HSFRI-PPy electrode to record the electrophysiological signal in comparison with commercial electrodes, including electrocardiogram (ECG), electromyography (EMG), and EEG (electroencephalography). Stable ECG signals were recorded by

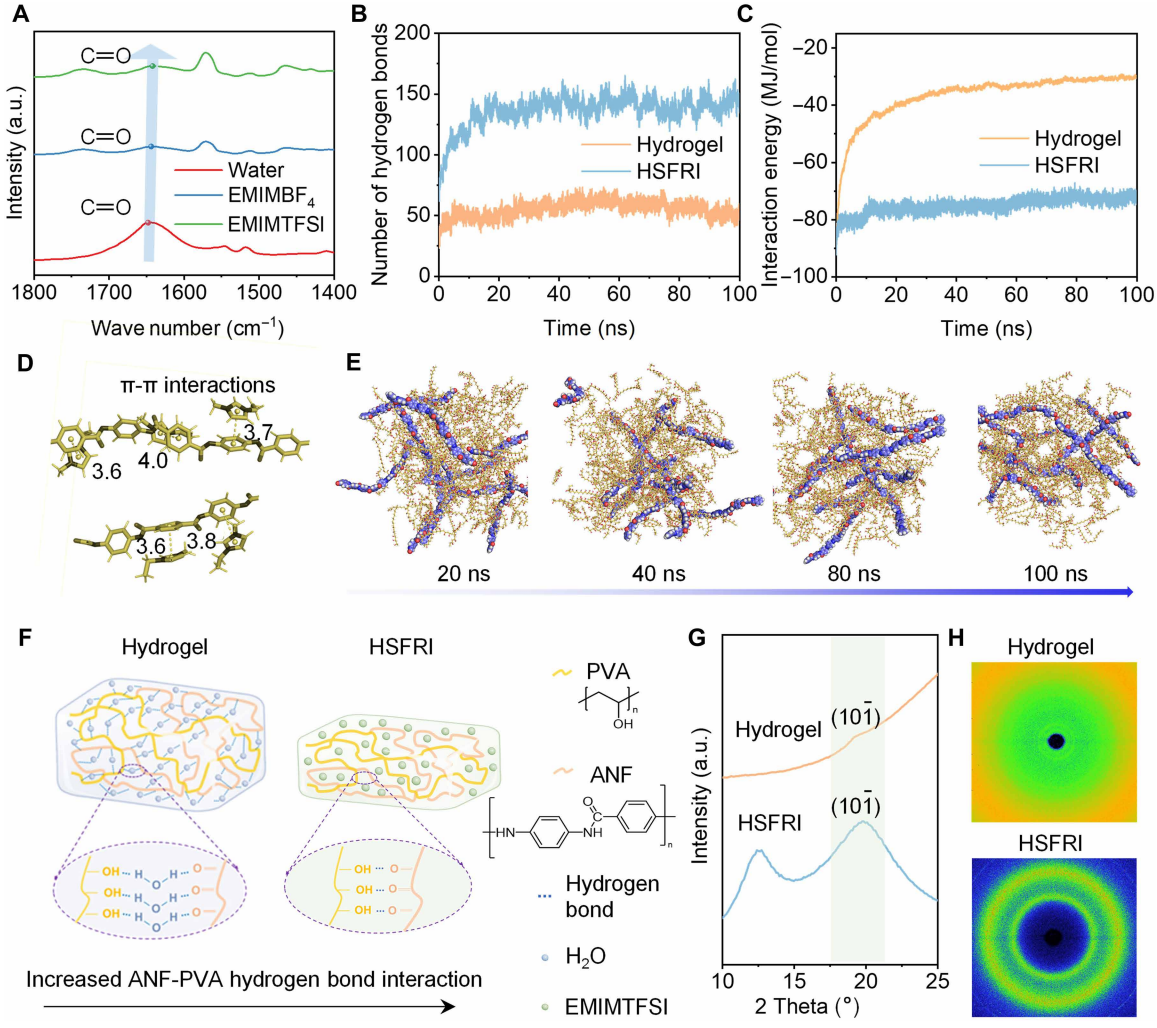

Fig. 3. Mechanistic analysis of solvent-engineered biphasic interfacial cohesion in HSFRIs. (**A**) FTIR spectra of gels prepared with different solvents, where a red shift in the carbonyl peak of ANFs indicates stronger hydrogen bonding with PVA. (**B**) Comparison of hydrogen bonding between ANF and PVA in hydrogels and HSFRIs, with increased hydrogen bond formation in HSFRIs facilitating biphasic interfacial cohesion. (**C**) Comparison of the total intermolecular interaction energy between the solvent and solute (ANF and PVA) in hydrogels and HSFRIs. Higher interaction energy in HSFRIs favors the retention of a high liquid fraction. (**D**) π-π interactions between the aromatic rings of EMIM and ANF. (**E**) Molecular dynamics simulation of the hydrogen bond formation process between ANF and PVA in HSFRIs. ANF and PVA gradually aggregate with the formation of hydrogen bonds. (**F**) Schematic illustration of the reinforcement mechanism, highlighting the formation of robust interfacial cohesion between ANF and PVA by more hydrogen bonds. (**G** and **H**) 1D curves (G) and 2D patterns (H) from WAXS characterization of hydrogels (top) and HSFRIs (bottom), indicating solvent-induced PVA crystallization in HSFRIs.

placing two electrodes on the chest. The HSFRI-PPy electrode captured signals with precise details and a signal-to-noise ratio (SNR) of 38.4 dB, comparable to the commercial electrode (37.8 dB). After exposure to the atmospheric environment for 24 hours, it maintained a stable EMG signal with an SNR of 22.8 dB, demonstrating its suitability for long-term use (Fig. 4, E and F, and fig. S20). High-quality EEG signals related to different muscle groups were collected using two pairs of HSFRI-PPy electrodes on the forearm. These signals were exploited for gesture recognition, highlighting their potential for human-machine interaction applications (Fig. 4F). EEG signals are inherently challenging to acquire because of their low amplitude, typically at the microvolt level. The HSFRI-PPy electrodes demonstrate the ability to record high-fidelity EEG signals that are comparable to those obtained using commercial electrodes in terms of SNR (Fig. 4G), spectral resolution (Fig. 4H), and power spectral density (Fig. 4I). All the EEG spectra exhibit a distinct alpha-band peak, indicative of a relaxed wakeful state. The HSFRI-PPy electrodes maintain their recording performance even after 24 hours of atmospheric exposure before use. We demonstrated a strain sensor based on the ionic conductivity of HSFRIs, enabling the detection of physiological motions such as smiling, joint bending, and speaking (fig. S22). The temperature dependence of HSFRIs' ionic conductivity enables excellent temperature sensing capabilities. The logarithm of conductivity exhibits a linear response to temperature, indicating their potential for wearable temperature sensors (fig. S23). In addition, monolithic HSFRI films with interdigitated PPy patterns function as symmetric planar supercapacitors, with PPy serving as the energy storage material and HSFRIs acting as the

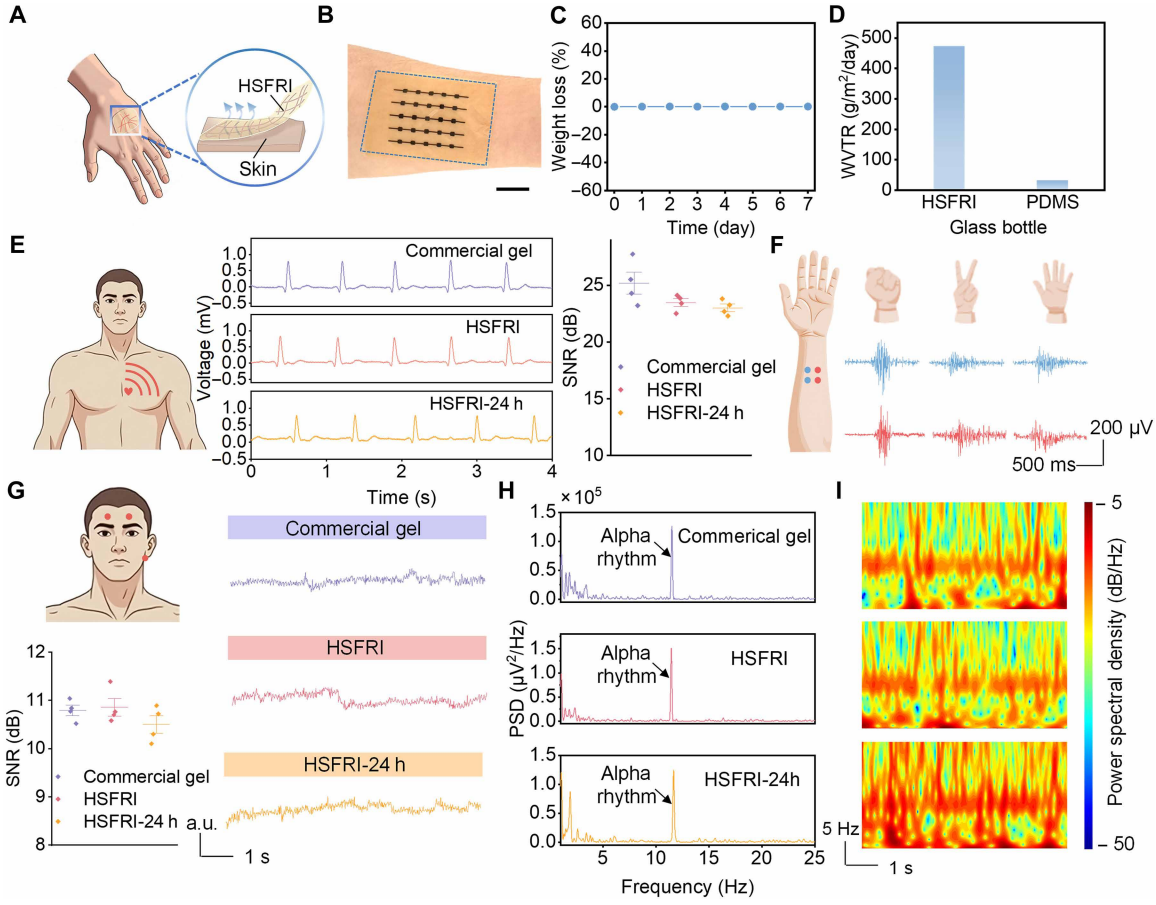

Fig. 4. On-skin bioelectronic interfaces based on HSFRIs. (**A**) Schematic illustration of a thin HSFRI-based electronic device adhered to the skin. (**B**) Photograph of an HSFRI-PPy electrode applied to the forearm. (**C**) Antidrying performance of HSFRIs. (**D**) Comparison of WVTR between HSFRI and PDMS of the same thickness, highlighting the superior gas permeability of HSFRI. (**E**) ECG signals recorded using a commercial gel electrode, a fresh HSFRI-PPy electrode, and an HSFRI-PPy electrode exposed to ambient conditions for 24 hours (h) (left), along with a comparison of their SNR (right). (**F**) Demonstration of gesture recognition based on EMG signals recorded by HSFRI-PPy electrodes. (**G**) EEG signals recorded using a commercial gel electrode, a fresh HSFRI-PPy electrode, and an HSFRI-PPy electrode after 2 hours of ambient exposure (right), with corresponding SNR comparison (left). (**H**) Distinct alpha rhythms recorded using a commercial gel electrode, a fresh HSFRI-PPy electrode, and an HSFRI-PPy electrode after 24 hours of ambient exposure. (**I**) Power spectral density comparison of EEG signals recorded with the same three types of electrodes. These results demonstrate that HSFRI-PPy electrodes exhibit performance on par with commercial counterparts.

electrolyte. These devices demonstrate a high areal capacitance of 9.06 mF/cm^2 and a low solution resistance (Rs) of 51.2 ohm (figs. S24 and S25), providing a promising solution for portable and wearable energy storage.

Applications in e-bandage

To demonstrate the potential application of HSFRIs for bioelectronic medicine, we explored their use as e-bandages to promote wound healing. As biomedical e-bandages, they need to be mechanically robust, antibacterial, capable of carrying drugs, biocompatible, and conductive to ensure compatibility with electrical stimulation (ES). HSFRIs, incorporating ionic liquids with ionic conductivity, provide significant advantages in meeting these requirements. The ionic conductivity of HSFRIs (6.5 mS/m) lies within the physiological range of human skin (0.01 to 260 mS/m) (*49*), which is sufficient to deliver electrical stimulation and accelerate wound healing in vivo effectively. The cationic nature of imidazole rings and the hydrophobicity of carbon chains disrupt bacterial cell membranes, leading to intracellular leakage and cell death (*49*). This imparts HSFRIs with excellent antibacterial properties, achieving a 100% antibacterial rate against both Gram-negative *Escherichia coli* (*E. coli*) and Gram-positive *Staphylococcus aureus* (*S. aureus*), significantly higher than that of hydrogels (fig. S26). Hydrogels face challenges in loading hydrophobic drugs like erythromycin (EM) due to their limited solubility. In contrast, EMIMTFSI effectively dissolves these drugs, allowing HSFRIs to serve as an effective platform for drug delivery (fig. S28). We assessed the biocompatibility of HSFRIs using the Cell Counting Kit-8 (CCK-8) assay with the NIH3T3 cell line. The high cell viability (~90%) after incubation with HSFRI extracts confirms their low cytotoxicity, making them suitable for biomedical applications (fig. S29).

We established a rat model of *S. aureus*–infected full-thickness skin defects (~5 mm in diameter) to evaluate the therapeutic efficacy of the HSFRIs e-bandage. The rats were randomly assigned to five groups and treated with phosphate-buffered saline (PBS) solution (blank control), HSFRIs, HSFRIs + ES, HSFRIs + EM, and HSFRIs + EM + ES. The wound healing process for all groups was monitored over a period of 9 days, progressing sequentially through four distinct stages: hemostasis, inflammation, proliferation, and

remodeling (Fig. 5, A and B). Compared to the blank control group, the group treated with HSFRIs exhibited less wound abscess formation, likely due to the antibacterial properties of HSFRIs. Quantitative analysis of the wound area further indicated that the combination of EM and ES accelerated the healing process (Fig. 5, C and D), as EM alleviated inflammation, while ES promoted cell proliferation and tissue regeneration. We assessed the microstructure of the wound after 9 days using hematoxylin and eosin (H&E) and Masson staining. ES treatment facilitated the regeneration of hair follicles and sebaceous glands, as well as increased collagen deposition, confirming an accelerated healing process (Fig. 5, E and F). Immunohistochemical analysis of various markers was performed on the 9th day to assess the recovery process and inflammatory response. In contrast to the controls, treatment with the HSFRIs e-bandage incorporating EM and ES showed higher expression levels of vascular endothelial growth factor (VEGF, a marker of angiogenesis) and α-smooth muscle actin (α-SMA, a marker for fibroblasts), as well as lower expression of interleukin-1B (IL-1β, a marker for inflammatory response) and IL-6 (a marker for acute phase reaction). These results demonstrate that treatment with the multifunctional HSFRIs

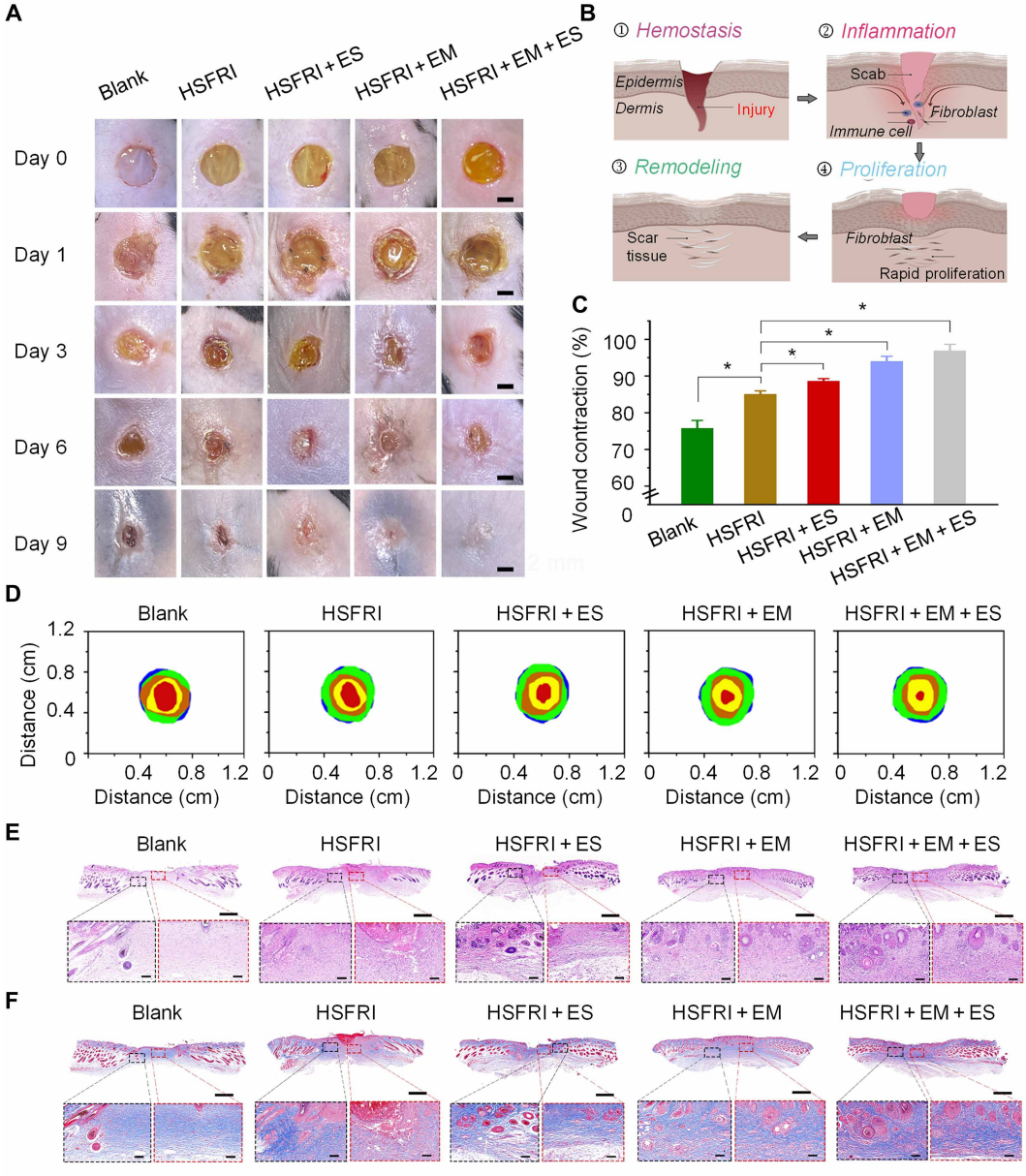

Fig. 5. E-bandage based on HSFRIs for wound healing. (**A**) Photographs showing full-thickness skin defect wounds treated with PBS solution, HSFRIs, HSFRIs + ES, HSFRIs + EM, and HSFRIs + EM + ES over 0, 1, 3, 6, and 9 days. Scale bars, 2 mm. (**B**) Schematic illustration of the wound healing process. (**C**) Wound contraction analysis of different treatment groups after 9 days. On the final day, the wound area in the control group and the HSFRI + EM + ES group had contracted by 75.74 and 96.84% of the initial wound area, respectively. (**D**) Quantitative evaluation of the wound healing progression. (**E** and **F**) Histological analysis on the 9th day of regenerated granulation tissue stained with H&E (E) and Masson's trichrome (F). $n = 5$, $^*P < 0.05$. Scale bars, (top row) 500 μm; (bottom) 100 μm.

e-bandage effectively promotes wound healing while reducing inflammation (fig. S30).

DISCUSSION

In summary, we have introduced mechanically robust ionogel materials as durable and multifunctional biomedical platforms. This work leverages the engineering of solvent-solute interactions as an effective strategy to regulate the microstructure and mechanical properties of gel materials. This approach facilitates the formation of a strongly bonded soft-hard phase interface, leading to exceptional strength and fracture energy. The underlying concept can be extended to other composite gel materials, unlocking possibilities for designing strong and tough materials. Beyond improving gel mechanics, this work also broadens the scope of iontronics in advanced diagnostics and therapies, such as regenerative medicine, tissue engineering, and electroceuticals. Expanding the selection of materials, including alternative solvents, polymer fibers, and matrices, could further enhance their achievable properties, creating valuable opportunities for advancements in soft robotics, biosensing, drug delivery, and a wide range of other applications.

MATERIALS AND METHODS

Fabrication of HSFRIs

The fabrication of HSFRIs involves a solvent exchange process. ANFs were prepared by dispersing 2 g of Kevlar para-aramid pulp and 2 g of KOH in 100 ml of DMSO, followed by continuous heating and stirring at 95°C for 7 days to yield a 2 wt % dispersion. The 2 wt % ANF dispersion and the 15 wt % PVA solution in DMSO were blended at an equal mass ratio to produce the precursor mixture. Blade coating was used to spread the liquid precursor onto a flat substrate, followed by immersion in EMIMTFSI for 24 hours to enable ionogel film formation. For comparison, the precursor was immersed in different liquids ($EMIMBF_4$ and water) to generate different gels swollen in different solvents. The solvent will be changed three times to ensure the removal of residual DMSO. The ANF-PVA ionogel was carefully detached from the substrate, yielding a freestanding ionogel film. To tailor the mechanical properties, ANF dispersions (1 to 3 wt %) were individually blended with 15 wt % PVA at equal mass ratios, resulting in ionogels with different compositions.

Fabrication of HSFRIs-PPy electrodes

PPy was in situ polymerized within the HSFRI matrix to establish well-defined electrical contacts by modifying our previously reported method (*50*). To achieve patterned conductivity, a flexible mask with predefined patterns was first fabricated using a high-precision laser-cutting technique. This mask was carefully aligned and placed onto the surface of the HSFRI to expose only the regions intended for polymerization. Subsequently, a reactive solution consisting of 0.5 mM ferric chloride ($FeCl_3$), serving as the oxidizing agent, and pyrrole monomer was dropped onto the surface in sequence. This method enabled the formation of highly localized, patterned conductive domains without affecting the surrounding regions, thus preserving the mechanical integrity and optical transparency of the HSFRI substrate. After polymerization, the patterned HSFRI-PPy electrode was thoroughly rinsed and immersed in EMIMTFSI for 48 hours. This soaking process ensured the complete removal of residuals. The supercapacitors were fabricated by integrating PPy electrodes with interlaced patterns onto the HSFRI.

Fabrication of EM-loaded e-bandages

To further enhance the wound healing capability of the HSFRIs, EM, a broad-spectrum macrolide antibiotic known for its effective antibacterial properties, was incorporated into the ionogel matrix. The EM-containing solvent was prepared by dissolving 0.1 g of EM in 10 ml of EMIMTFSI. Then, the liquid precursor, consisting of ANFs and PVA at a mass ratio of 2:15, was subjected to a solvent exchange process with the EM-loaded EMIMTFSI solution. This process enabled the efficient loading of EM into the polymer matrix through physical absorption. To ensure complete removal of the original DMSO solvent, which may pose cytotoxic effects in biological environments, the EM-containing solvent was replaced three times during the solvent exchange step. This repeated replacement not only facilitated thorough DMSO elimination but also enhanced the loading efficiency and uniform distribution of EM throughout the ionogel matrix.

Molecular dynamics simulation

The molecular dynamics simulations were performed using Gromacs 2022.4. The force field of simulation systems was GAFF. The water molecule model used was TIP3P, and the dimensions of the water box were set to 8.0 nm by 8.0 nm by 8.0 nm. The 3D structures of ANF, PVA, EMIM, and TFSI molecules were constructed using ChemOffice. Geometry optimization was performed using Gaussian16 with the B3LYP functional and the 6-31G(d) basis set (*51*). The corresponding restrained electrostatic potential (RESP) charges were generated using Multiwfn (*52*). The optimized structures obtained from Gaussian16 were then used to generate topology files with sobtop, which were subsequently applied in molecular dynamics simulations. Ten ANF molecules and 186 PVA molecules were randomly inserted into both the aqueous and ionic liquid systems. After constructing the initial configurations of both the aqueous and ionic liquid systems, a two-step energy minimization was performed. The first step used the steepest descent algorithm for 10,000 steps, followed by the conjugate gradient algorithm for 5000 steps. After energy optimization, a 200-ps equilibration was conducted under the isothermal–isobaric (NPT) ensemble (constant number of particles, pressure, and temperature). Subsequently, a 100-ns production simulation was carried out. The V-rescale thermostat was used for temperature control, and the Parrinello-Rahman algorithm was applied for pressure coupling. The simulation time step was 2 fs, and the system temperature was maintained at 300 K. Electrostatic interactions were calculated using the particle mesh Ewald method, with cutoff distances for both Coulombic and van der Waals interactions set to 12 Å. Hydrogen bonds were constrained using the LINCS algorithm. Conformations were saved every 10 ps. Simulation results were visualized using the built-in tools of GROMACS and PyMOL.

Material and mechanical characterizations

The microstructures were examined using SEM (Hitachi S4800 FEG). For SEM sample preparation, the materials were first fractured in liquid nitrogen to preserve structural integrity, followed by drying through critical point drying (Tousimis Autosamdri 931). The chemical composition and functional groups were analyzed using FTIR spectroscopy (Thermo Fisher Scientific, IS50).

Electrochemical characterization was performed by an electrochemical station (Autolab Pgstat 302 N). The areal capacitance (C) was calculated using the following equation

$$C = I \times t/(A \times V)$$

where I is the discharge current, t is the discharge time, A represents the electrode surface area, and V denotes the voltage window.

Tensile experiments were performed at ambient temperature using a mechanical testing machine (Zwick Roell) under a constant strain rate of 100% per minute. Engineering stress-strain curves were recorded, and the tensile modulus was calculated as the stress-to-strain ratio at a strain of 5% ($\varepsilon = 5\%$). To evaluate the fracture energy, tensile tests were carried out on both notched and unnotched specimens. The fracture energy was then calculated by comparing the results of these two types of samples, following a widely accepted approach *(48)*.

Evaluation of permeability and antidrying performance

The WVTR was measured to evaluate the permeability of the samples. Each sample was cut into a circular shape and sealed over the opening of a glass bottle with a 1-cm diameter, which contained deionized water. The assembled diffusion cells were then placed in a controlled environment chamber maintained at 70% relative humidity and 15°C for 24 hours. The weight of each bottle was recorded at hourly intervals. *WVTR* was calculated using the following equation

$$WVTR = \left(W_0 - W\right)/(A \times t)$$

where W_0 is the initial weight, W is the weight after a specific time t, and A represents the surface area available for vapor transmission.

To evaluate water retention performance, the samples were exposed to ambient conditions for 7 days. The degree of dehydration was determined by the equation

$$\text{Weight loss}(\%) = \left(W_0 - W\right) * 100\%/W_0$$

where W_0 and W denote the initial and final weights of the material after exposure, respectively.

Epidermal physiological recordings

All physiological experiments were conducted following standardized procedures, with informed consent obtained from all participants and ethical approval granted by the Human Research Ethics Committee of The University of Hong Kong (EA200171). ECG monitoring was performed by placing a pair of HSFRI-PPy electrodes on the volunteer's chest, and the signals were recorded using a commercial device (PowerLab T26, AD Instruments). EMG signals were acquired by attaching two pairs of HSFRI-PPy electrodes to the forearm. EEG signals were recorded using the RZ5D BioAmp Processor (Tucker-Davis Technologies, USA) by placing two HSFRI-PPy electrodes on the forehead, with a commercial electrode placed near the ear serving as the reference electrode. Before all the experiments, the skin surface was cleaned using alcohol swabs.

Biocompatibility characterizations

The extract solution of the HSFRI ionogel was prepared by immersing 30 mg of the gel in 3 ml of culture medium for 72 hours. NIH3T3 cells (mouse embryonic fibroblasts) were seeded into 96-well plates at a density of 5×10^3 cells per well using Dulbecco's modified Eagle's medium supplemented with 10% fetal bovine serum and incubated for 24 hours. Afterward, the culture medium was replaced with the ionogel extract with different dilution ratios, and the cells were further cultured for an additional 24 hours. Cell viability was assessed using the CCK-8 assay. Following removal of the extract, 150 μl of fresh medium containing 10% CCK-8 reagent was added to each well and incubated for another 2 hours. The cell viability (%) was calculated as follows

$$\text{Cell viability} = A_{\text{sample}}/A_{\text{control}}$$

where A_{sample} and A_{control} represent the absorbance at 450 nm for the experimental and negative control groups, respectively, (with the control group consisting of cells cultured in untreated medium).

Antibacterial tests

Ten microliters of a bacterial suspension [10^7 colony-forming unit (CFU) ml^{-1}] was carefully dropped onto the surface of each sample. A circular polyethylene terephthalate membrane (0.5 cm in diameter) was then placed over the droplet to ensure full contact between the bacteria and the sample surface, as well as to minimize evaporation. The samples were incubated at 37°C for 3 hours in a constant-temperature incubator. After incubation, 2 ml of PBS was added for *S. aureus* and 4 ml for *E. coli*. The plates were then subjected to ultrasonication for 6 min to detach bacteria from the sample surfaces. Next, 200 μl of the *S. aureus* suspension and 150 μl of the *E. coli* suspension were plated onto LB-agar media and evenly spread using sterile glass beads. The plates were incubated at 37°C for 12 to 16 hours. The bacterial colonies were counted to calculate the sterilization efficiency.

Full-layer skin defect–infected model

All animal studies were performed by Shenzhen Lingfu Top Biotechnology Co. Ltd. and approved by the Ethical Committee of the Animal Experimental Center (No. NS20240333). In this study, female C57BL/6 mice (6 to 8 weeks old, healthy, without skin lesions) were used. Mice were anesthetized with isoflurane inhalation, and the dorsal hair was removed using depilatory cream, followed by cleaning with sterile cotton swabs and disinfection with povidone-iodine and ethanol. A 5-mm diameter full-thickness skin defect was created on the dorsum with a biopsy punch. HSFRI discs of the same diameter were immediately applied to the wound. After anesthetizing with pentobarbital sodium (50 mg/kg), the animals were placed on a 37°C heating pad, and their back hair was removed using hair-removal agents. Afterward, the back skin of animals was removed by a Biopunch (diameter, 5 mm), and then 100 μl of *S. aureus* suspension (density 1×10^6 CFU/ml) was applied on the wound to create the infected model. After surgery, the mice were returned to their cages for recovery and routine monitoring. The mice were divided into five groups ($n = 5$ per group) and were fasted for 24 hours before surgery. These five groups were (i) blank control (treated with PBS), (ii) HSFRIs, (iii) HSFRIs + ES, (iv) HSFRIs + EM, and (v) HSFRIs + EM + ES. Wound states in each group were observed on day 1, day 3, day 6, and day 9. For groups receiving EM, HSFRIs preloaded with EM were directly applied to the wound surface to achieve local drug delivery. For ES therapy on the wounds, we used the commercialized electric needles (SDZ-II, Hwato) to administer the treatment. The pulse-shaped electric field (30 V, 0.2-ms pulse duration, continuously asymmetric bipolar pulse) was delivered on days 1, 3, 5, and 7, each session lasting 20 min.

Histological and immunohistochemical staining analysis

After 10-day monitoring, the tissues from wound sites were excised and fixed in 4% paraformaldehyde for 24 hours and then subjected to H&E and Masson trichromatic staining as well as immunohistochemical staining analysis. After fixation, the collected samples were dehydrated, embedded into paraffin, and sectioned into 6-μm sections. Then, these thin sections were stained with H&E and Masson's trichrome and imaged using optical microscopy. For immunohistochemical staining, the paraffin-embedded tissue sections were deparaffinized in xylene and gradually rehydrated in an ethanol series. Antigen retrieval was conducted using microwave heating. Nonspecific antigens were blocked with 1.5% normal goat serum. Slides were left to incubate overnight with primary antibodies (CD31, VEGF, and α-SMA; IL-1β, IL-6, and tumor necrosis factor–α) for a 1:1000 dilution at 4°C, followed by incubation with secondary antibodies. The sections were stained with diaminobenzidine, counterstained with hematoxylin, dehydrated, and then cleared.

Statistical analyses

All experimental results were run in triplicate unless otherwise specified. Numerical data were expressed as means ± SD. Statistical analysis was performed by GraphPad Prism 6.0 software, and the statistical differences were determined using one-way analysis of variance (ANOVA).

Supplementary Materials

This PDF file includes:

Figs. S1 to S30
Tables S1 and S2

REFERENCES AND NOTES

1. L. Chen, C. Zhao, J. Huang, J. Zhou, M. Liu, Enormous-stiffness-changing polymer networks by glass transition mediated microphase separation. *Nat. Commun.* **13**, 6821 (2022).
2. C. Christianson, N. N. Goldberg, D. D. Deheyn, S. Cai, M. T. Tolley, Translucent soft robots driven by frameless fluid electrode dielectric elastomer actuators. *Sci. Robot.* **3**, eaat1893 (2018).
3. Z. Zhang, L. Qian, J. Cheng, C. Ma, G. Zhang, Neural network-inspired polyurea ionogel with mechanical robustness, low hysteresis, and high transparency for soft iontronics. *Adv. Funct. Mater.* **34**, 2402115 (2024).
4. X. Xiao, M. Wang, S. Chen, Y. Zhang, H. Gu, Y. Deng, G. Yang, C. Fei, B. Chen, Y. Lin, M. D. Dickey, J. Huang, Lead-adsorbing ionogel-based encapsulation for impact-resistant, stable, and lead-safe perovskite modules. *Sci. Adv.* **7**, eabi8249 (2021).
5. W. Zhao, Y. Zheng, M. Jiang, T. Sun, A. Huang, L. Wang, W. Jiang, Q. Zhang, Exceptional n-type thermoelectric ionogels enabled by metal coordination and ion-selective association. *Sci. Adv.* **9**, eadk2098 (2023).
6. S. Liu, Y. Yang, H. Huang, J. Zheng, G. Liu, T. H. To, B. Huang, Giant and bidirectionally tunable thermopower in nonaqueous ionogels enabled by selective ion doping. *Sci. Adv.* **8**, eabj3019 (2022).
7. S. Wan, W. Ma, Y. Wang, Y. Xiao, S. Chen, Electrolytes design for extending the temperature adaptability of lithium-ion batteries: From fundamentals to strategies. *Adv. Mater.* **36**, e2311912 (2024).
8. S. J. Hong, Y. R. Lee, A. Bag, H. S. Kim, T. Q. Trung, M. J. Sultan, D.-B. Moon, N.-E. Lee, Bio-inspired artificial mechanoreceptors with built-in synaptic functions for intelligent tactile skin. *Nat. Mater.* **24**, 1100–1108 (2025).
9. C. Jiang, J. Fu, H. Zhang, Y. Hua, L. Cao, J. Ren, M. Zhou, F. Jiang, X. Jiang, S. Ling, Self-reinforcing ionogel bioadhesive interface for robust integration and monitoring of bioelectronic devices with hard tissues. *Adv. Mater.* **37**, e2413028 (2024).
10. X. Fan, S. Liu, Z. Jia, J. J. Koh, J. C. C. Yeo, C.-G. Wang, N. E. Surat'man, X. J. Loh, J. Le Bideau, C. He, Z. Li, T.-P. Loh, Ionogels: Recent advances in design, material properties and emerging biomedical applications. *Chem. Soc. Rev.* **52**, 2497–2527 (2023).
11. Y. Wu, Y. Li, Y. Liu, D. Zhu, S. Xing, N. Lambert, H. Weisbecker, S. Liu, B. Davis, L. Zhang, M. Wang, G. Yuan, C. Z. You, A. Zhang, C. Duncan, W. Xie, Y. Wang, Y. Wang, S. Kanamurlapudi, G.-G. Evert, A. Putcha, M. D. Dickey, K. Huang, W. Bai, Orbit symmetry breaking in MXene implements enhanced soft bioelectronic implants. *Sci. Adv.* **10**, eadp8866 (2024).
12. Y. He, Y. Cheng, C. Yang, C. F. Guo, Creep-free polyelectrolyte elastomer for drift-free iontronic sensing. *Nat. Mater.* **23**, 1107–1114 (2024).
13. H. Ye, B. Wu, S. Sun, P. Wu, Self-compliant ionic skin by leveraging hierarchical hydrogen bond association. *Nat. Commun.* **15**, 885 (2024).
14. D. Lv, X. Li, X. Huang, C. Cao, L. Ai, X. Wang, S. K. Ravi, X. Yao, Microphase-separated elastic and ultrastretchable ionogel for reliable ionic skin with multimodal sensation. *Adv. Mater.* **36**, e2309821 (2024).
15. W. Zhao, H. Zhou, Y. Lu, J. Jiang, L. Zhao, Radiation controllable construction of multifunctional ionogel with a soft-rigid structure for high-performance ionic skin. *Cell Rep. Phys. Sci.* **5**, 102107 (2024).
16. Q.-F. Guan, H.-B. Yang, Z.-M. Han, Z.-C. Ling, C.-H. Yin, K.-P. Yang, Y.-X. Zhao, S.-H. Yu, Sustainable cellulose-nanofiber-based hydrogels. *ACS Nano* **15**, 7889–7898 (2021).
17. X. Lyu, K. Yu, H. Zhang, P. Zhou, Z. Shen, Z. Zou, Tough fiber-reinforced composite ionogels with crack resistance surpassing metals. *Nat. Commun.* **16**, 4005 (2025).
18. N. Zhang, Z. Liu, Q. Yu, X. Li, Y. Zhu, S. Wang, Y. Hao, B. Jiang, Z. Zhang, R. O. Ritchie, On the damage tolerance of bioinspired gradient composites with nacre-like architecture. *Adv. Funct. Mater.* **35**, 2421057 (2025).
19. G. Zeng, Y. Dong, J. Luo, Y. Zhou, C. Li, K. Li, X. Li, J. Li, Desirable strong and tough adhesive inspired by dragonfly wings and plant cell walls. *ACS Nano* **18**, 9451–9469 (2024).
20. W. Woigk, E. Poloni, M. Grossman, F. Bouville, K. Masania, A. R. Studart, Nacre-like composites with superior specific damping performance. *Proc. Natl. Acad. Sci. U.S.A.* **119**, e2118868119 (2022).
21. R. O. Ritchie, The conflicts between strength and toughness. *Nat. Mater.* **10**, 817–822 (2011).
22. H. Dinh Xuan, B. Timothy, H.-Y. Park, T. N. Lam, D. Kim, Y. Go, J. Kim, Y. Lee, S. I. Ahn, S.-H. Jin, J. Yoon, Super stretchable and durable electroluminescent devices based on double-network ionogels. *Adv. Mater.* **33**, e2008849 (2021).
23. R. Zhu, D. Zhu, Z. Zheng, X. Wang, Tough double network hydrogels with rapid self-reinforcement and low hysteresis based on highly entangled networks. *Nat. Commun.* **15**, 1344 (2024).
24. M. Wang, P. Zhang, M. Shamsi, J. L. Thelen, W. Qian, V. K. Truong, J. Ma, J. Hu, M. D. Dickey, Tough and stretchable ionogels by in situ phase separation. *Nat. Mater.* **21**, 359–365 (2022).
25. R. Zhou, Y. Jin, Y. Li, H. Jin, W. Zeng, J. Mei, Y. Liu, In-situ phase separation constructing robust hydrophobic ionogels with multifunction. *Chem. Eng. J.* **476**, 146840 (2023).
26. B. Bao, Q. Zeng, K. Li, J. Wen, Y. Zhang, Y. Zheng, R. Zhou, C. Shi, T. Chen, C. Xiao, B. Chen, T. Wang, K. Yu, Y. Sun, Q. Lin, Y. He, S. Tu, L. Zhu, Rapid fabrication of physically robust hydrogels. *Nat. Mater.* **22**, 1253–1260 (2023).
27. M. Wang, X. Xiao, S. Siddika, M. Shamsi, E. Frey, W. Qian, W. Bai, B. T. O'Connor, M. D. Dickey, Glassy gels toughened by solvent. *Nature* **631**, 313–318 (2024).
28. P. A. Hunt, C. R. Ashworth, R. P. Matthews, Hydrogen bonding in ionic liquids. *Chem. Soc. Rev.* **44**, 1257–1288 (2015).
29. T. Zhou, H. Yuk, F. Hu, J. Wu, F. Tian, H. Roh, Z. Shen, G. Gu, J. Xu, B. Lu, X. Zhao, 3D printable high-performance conducting polymer hydrogel for all-hydrogel bioelectronic interfaces. *Nat. Mater.* **22**, 895–902 (2023).
30. Q. Liu, X. Dong, H. Qi, H. Zhang, T. Li, Y. Zhao, G. Li, W. Zhai, 3D printable strong and tough composite organo-hydrogels inspired by natural hierarchical composite design principles. *Nat. Commun.* **15**, 3237 (2024).
31. M. Zhang, L. Zhao, F. Tian, X. Zhao, Y. Zhang, X. Yang, W. Huang, R. Yu, Bionic artificial skin based on self-healable ionogel composites with tailored mechanics and robust interfaces. *Adv. Mater.* **36**, 2405776 (2024).
32. W. Li, L. Li, S. Zheng, Z. Liu, X. Zou, Z. Sun, J. Guo, F. Yan, Recyclable, healable, and tough ionogels insensitive to crack propagation. *Adv. Mater.* **34**, 2203049 (2022).
33. L. Li, X. Wang, S. Gao, S. Zheng, X. Zou, J. Xiong, W. Li, F. Yan, High-toughness and high-strength solvent-free linear poly(ionic liquid) elastomers. *Adv. Mater.* **36**, 2308547 (2024).
34. L. Li, W. Li, X. Wang, X. Zou, S. Zheng, Z. Liu, Q. Li, Q. Xia, F. Yan, Ultra-tough and recyclable ionogels constructed by coordinated supramolecular solvents. *Angew. Chem. Int. Ed. Engl.* **61**, e202212512 (2022).
35. J. Kim, G. Zhang, M. Shi, Z. Suo, Fracture, fatigue, and friction of polymers in which entanglements greatly outnumber cross-links. *Science* **374**, 212–216 (2021).
36. H. Jiang, F. Xie, J. Wang, N. F. Attia, C. Xiong, P. Qiu, S. Jiang, G. Li, Tough, crack-resistant ionogels based on chain entanglement structures for health monitoring applications. *ACS Appl. Polym. Mater.* **7**, 7899–7909 (2025).
37. J. Li, Z. Suo, J. J. Vlassak, Stiff, strong, and tough hydrogels with good chemical stability. *J. Mater. Chem. B* **2**, 6708–6713 (2014).
38. M. Hua, S. Wu, Y. Ma, Y. Zhao, Z. Chen, I. Frenkel, J. Strzalka, H. Zhou, X. Zhu, X. He, Strong tough hydrogels via the synergy of freeze-casting and salting out. *Nature* **590**, 594–599 (2021).

39. C. Shan, M. Che, A. Cholewinski, R. Su, B. Zhao, Multifunctional nanocrystalline cellulose ionogels toward tough and sustainable materials. *Cell Rep. Phys. Sci.* **4**, 102511 (2023).
40. M. Wang, S. Sun, G. Dong, F. Long, J. T. Butcher, Soft, strong, tough, and durable protein-based fiber hydrogels. *Proc. Natl. Acad. Sci. U.S.A.* **120**, e2213030120 (2023).
41. J.-Y. Sun, X. Zhao, W. R. K. Illeperuma, O. Chaudhuri, K. H. Oh, D. J. Mooney, J. J. Vlassak, Z. Suo, Highly stretchable and tough hydrogels. *Nature* **489**, 133–136 (2012).
42. J. P. Gong, Why are double network hydrogels so tough? *Soft Matter* **6**, 2583–2590 (2010).
43. P. H. Corkhill, A. S. Trevett, B. J. Tighe, The potential of hydrogels as synthetic articular cartilage. *Proc. Inst. Mech. Eng. H* **204**, 147–155 (1990).
44. K. Cao, X. Ma, B. Zhang, Y. Wang, Y. Wang, Tensile behavior of polycarbonate over a wide range of strain rates. *Mater. Sci. Eng. A* **527**, 4056–4061 (2010).
45. H. S. Ku, D. Baddeley, C. Snook, C. S. Chew, Fracture toughness of vinyl ester composites cured by microwave irradiation: Preliminary results. *J. Reinf. Plast. Compos.* **24**, 1181–1201 (2005).
46. H. Liu, H. Li, Z. Wang, X. Wei, H. Zhu, M. Sun, Y. Lin, L. Xu, Robust and multifunctional kirigami electronics with a tough and permeable aramid nanofiber framework. *Adv. Mater.* **34**, e2207350 (2022).
47. W. Li, X. Wang, Z. Liu, X. Zou, Z. Shen, D. Liu, L. Li, Y. Guo, F. Yan, Nanoconfined polymerization limits crack propagation in hysteresis-free gels. *Nat. Mater.* **23**, 131–138 (2024).
48. L. Xu, X. Zhao, C. Xu, N. A. Kotov, Water-rich biomimetic composites with abiotic self-organizing nanofiber network. *Adv. Mater.* **30**, 1703343 (2018).
49. C.-C. Yan, W. Li, Z. Liu, S. Zheng, Y. Hu, Y. Zhou, J. Guo, X. Ou, Q. Li, J. Yu, L. Li, M. Yang, Q. Liu, F. Yan, Ionogels: Preparation, properties and applications. *Adv. Funct. Mater.* **34**, 2314408 (2024).
50. H. He, H. Li, A. Pu, W. Li, K. Ban, L. Xu, Hybrid assembly of polymeric nanofiber network for robust and electronically conductive hydrogels. *Nat. Commun.* **14**, 759 (2023).
51. M. J. Frisch, G. W. Trucks, H. B. Schlegel, G. E. Scuseria, M. A. Robb, J. R. Cheeseman, G. Scalmani, V. Barone, G. A. Petersson, H. Nakatsuji, X. Li, M. Caricato, A. V. Marenich, J. Bloino, B. G. Janesko, R. Gomperts, B. Mennucci, H. P. Hratchian, J. V. Ortiz, A. F. Izmaylov, J. L. Sonnenberg, Williams, F. Ding, F. Lipparini, F. Egidi, J. Goings, B. Peng, A. Petrone, T. Henderson, D. Ranasinghe, V. G. Zakrzewski, J. Gao, N. Rega, G. Zheng, W. Liang, M. Hada, M. Ehara, K. Toyota, R. Fukuda, J. Hasegawa, M. Ishida, T. Nakajima, Y. Honda, O. Kitao, H. Nakai, T. Vreven, K. Throssell, J. A. Montgomery Jr., J. E. Peralta, F. Ogliaro, M. J. Bearpark, J. J. Heyd, E. N. Brothers, K. N. Kudin, V. N. Staroverov, T. A. Keith, R. Kobayashi, J. Normand, K. Raghavachari, A. P. Rendell, J. C. Burant, S. S. Iyengar, J. Tomasi, M. Cossi, J. M. Millam, M. Klene, C. Adamo, R. Cammi, J. W. Ochterski, R. L. Martin, K. Morokuma, O. Farkas, J. B. Foresman, D. J. Fox. (Wallingford, CT, 2016).
52. T. Lu, F. Chen, Multiwfn: A multifunctional wavefunction analyzer. *J. Comput. Chem.* **33**, 580–592 (2012).
53. X. Zhao, B. Guo, H. Wu, Y. Liang, P. X. Ma, Injectable antibacterial conductive nanocomposite cryogels with rapid shape recovery for noncompressible hemorrhage and wound healing. *Nat. Commun.* **9**, 2784 (2018).

Acknowledgments

Funding: L.X. acknowledge funding support from Research Grants Council (RGC) of Hong Kong (Project 17200722, 17201523, 17209524, and C6004-22Y) and National Natural Science Foundation of China (Project T2522029). This study was also supported by the InnoHK initiative of the Innovation and Technology Commission of the Hong Kong Special Administrative Region Government. **Author contributions:** Conceptualization: H.Z. and L.X. Methodology: H.Z., W.J., and M.S. Investigation: H.Z., W.J., M.S., Y.C., X.Z., H.L., and X.H. Visualization: H.Z., W.J., and M.S. Supervision: L.X. and P.S. Writing—original draft: H.Z. and L.X. Writing—review and editing: H.Z., L.X., and P.S. **Competing interests:** The authors declare that they have no competing interests. **Data and materials availability:** All data needed to evaluate the conclusions in the paper are present in the paper and/or the Supplementary Materials.

Submitted 18 July 2025
Accepted 24 October 2025
Published 19 November 2025
10.1126/sciadv.aea6883